Biomicrofluidics ARTICLE scitation.org/journal/bmf

Adhesive bonding strategies to fabricate high-strength and transparent 3D printed microfluidic device

Cite as: Biomicrofluidics 14, 024113 (2020); doi: 10.1063/5.0003302
Submitted: 3 February 2020 · Accepted: 9 April 2020 ·
Published Online: 20 April 2020

View Online Export Citation CrossMark

Seren Kecili and H. Cumhur Tekin[a)]

AFFILIATIONS

Department of Bioengineering, Izmir Institute of Technology, Urla, Izmir 35430, Turkey

[a)]**Author to whom correspondence should be addressed:** cumhurtekin@iyte.edu.tr. **Tel.:** +90 232 750 7388. **Fax:** +90 232 750 6505

ABSTRACT

Recently, the use of 3D printing technologies has become prevalent in microfluidic applications. Although these technologies enable low-cost, rapid, and easy fabrication of microfluidic devices, fabricated devices suffer from optical opaqueness that inhibits their use for microscopic imaging. This study investigates bonding strategies using polydimethylsiloxane (PDMS) and printer resin as interlayer materials to fabricate high-strength optically transparent 3D-printed microfluidic devices. First, we fabricated microfluidic structures using a stereolithography 3D printer. We placed 3D-printed structures on interlayer materials coated surfaces. Then, we either let these 3D-printed structures rest on the coated slides or transferred them to new glass slides. We achieved bonding between 3D-printed structures and glass substrates with UV exposure for resin and with elevated temperature for PDMS interlayer materials. Bonding strength was investigated for different interlayer material thicknesses. We also analyzed the bright-field and fluorescence imaging capability of microfluidic devices fabricated using different bonding strategies. We achieve up to twofold (9.1 bar) improved bonding strength and comparable fluorescence sensitivity with respect to microfluidic devices fabricated using the traditional plasma activated PDMS-glass bonding method. Although stereolithography 3D printer allows fabrication of enclosed channels having dimensions down to ~600 μm, monolithic transparent microfluidic channels with $280 \times 110\,\mu m^2$ cross section can be realized using adhesive interlayers. Furthermore, 3D-printed microfluidic chips can be integrated successfully with Protein-G modified substrates using resin interlayers for detection of fluorescent-labeled immunoglobulin down to ~30 ng/ml. Hence, this strategy can be applied to fabricate high-strength and transparent microfluidic chips for various optical imaging applications including biosensing.

Published under license by AIP Publishing. https://doi.org/10.1063/5.0003302

I. INTRODUCTION

Microfluidic devices are fabricated using several techniques, such as micro-machining,[1] hot embossing,[2] and more frequently replica molding using soft lithography.[3] In the soft lithography technique, microfluidic devices are prototyped in polydimethylsiloxane (PDMS) by using a high precision mold, which is generally fabricated in a cleanroom environment with expensive tools and reagents and labor intensive process.[4–6] Multiple microfabrications and PDMS layer processing steps are required to fabricate three dimensional (3D) microfluidic structures using soft lithography technique that limits device designs and also increases device fabrication time and cost.[7–10] However, 3D printing technology, alternative to traditional fabrication methods, provides a rapid prototyping of microfluidic devices with tailored 3D channel features.[11] 3D printers can be deployed in a laboratory environment with a low capital investment (<3500$) that allows low-cost fabrication of microfluidic devices without using expensive infrastructures.[12] Different technologies, such as laser sintering, laser melting, electron beam melting, laminated object manufacturing, etc., are available for 3D printers, but stereolithography (SLA), multi-jet printing (MJM), and fused deposition modeling (FDM) are generally used to fabricate microfluidic devices due to their high resolution and printed material diversity.[11–15]

3D printing technologies have been applied in microfluidic devices for several different biological applications.[16–18] These devices are either fabricated directly on 3D printers or replicated

Published under license by AIP Publishing.

using 3D-printed molds. Although direct printing allows easy fabrication of complex channel geometries, its optical transparency is limited for microscopy imaging purposes.[19–20] Mechanical polishing can help to enhance optical clarity of exterior surfaces of 3D-printed structures, but transparency of inner surfaces does not change with this process.[21] To enhance transparency, inner surfaces of printed channels can be coated with polymers, which requires long processing time (≥1 day).[21] Adjusting printing process parameters can also boost the transparency of printed channels with dimensions down to 400 μm.[22] Moreover, implementation of different printer resin formulations, such as Watershed XC 11122, fluorinated perfluoropolyether (PFPE) methacrylates, and poly (ethylene glycol) diacrylate (PEGDA) based formulations can bring only a limited improvement in optical clarity.[23–26] Coating exterior surfaces of printed devices with a fluid whose reflective index is matched with the resin has been shown to improve transparency of channels.[23] Transparent microfluidic channels have also been printed on a glass slide with an SLA printer using custom-made 3D printable PDMS resin, which requires several seconds for curing a single printing layer.[27] Microfluidic devices can be also printed using silica nanoparticles mixed with a UV curable monomer, but 3D-printed structures need to be sintered at high temperature (>1000 °C) to create transparent fused silica glass devices.[28] Furthermore, optically clear substrates can be used to seal 3D-printed open channels via clamping to enhance optical transparency of the channels.[29] However, sealed channels can only withstand low hydrostatic pressures. 3D-printed substrates can be also bonded on transparent substrates (e.g., glass, PDMS, etc.) by heating substrates above the glass transition temperature of 3D printer resin, which permanently deforms the resin.[4] Furthermore, 3D-printed microfluidic channels can be bonded on PDMS substrates using different intermediate layers such as a double-sided tape, PDMS/tape composite, UV glue, (3-aminopropyl)triethoxysilane (APTES), and sputter-coated silicon dioxide that results in 4.36 bar maximum burst pressure.[30] Additionally, microfluidic devices can also be directly printed on various functionalized (e.g., silanized) substrates that can withstand up to 1.1 bar pressure.[31] Silanization can also be used to bond SLA epoxy-based resin to PDMS at room temperature with a bonding strength of 3.5 bar.[32] Moreover, 3D-printed microfluidic devices can be bonded to flexible substrates using UV curable ink that can withstand up to 1 bar burst pressure.[33]

This study explores adhesive bonding strategies to fabricate high-strength transparent 3D-printed microfluidic devices for use in imaging applications. For this purpose, we bonded open channels printed using SLA technology on glass slides with adhesive interlayers, which are PDMS and commercial resin (Formlabs Clear Resin FLGPCL02). These strategies allow similar optical properties for bright-field/fluorescence microscopy imaging and improved bonding strength compared to traditional plasma bonded PDMS/glass microfluidic devices. Furthermore, this fabrication strategy obtains smaller channel dimensions than direct 3D printing of enclosed microfluidic channels. 3D-printed microfluidic channels can be also easily integrated with protein-modified surfaces using adhesive interlayers for fluorescent-based protein detection. Hence, the adhesive bonding strategy enhances the transparency of 3D-printed microfluidic devices for various microscopy imaging applications.

II. MATERIALS AND METHODS

A. 3D Printing of microfluidic channels

Designed channels are printed using a Formlabs Form 2 SLA 3D printer (Formlabs, USA) in a high-resolution mode. In this process, channel designs are tilted 30°, support structures are added to each design using printer slicer program (Preform), and channels are fabricated using UV curable Formlabs Clear Resin (FLGPCL02, Formlabs, USA). After the printing process, all 3D-printed structures are washed twice in isopropanol (VWR International, USA) for 10 min, and then supports are cleared manually.

B. Bonding of 3D-printed structures on a glass substrate

We employed adhesive bonding to seal 3D-printed microfluidic channels on a glass slide with different interlayer materials (Fig. 1). To do so, we first cleaned glass slides (Marienfeld, Germany) with 70% ethanol (K50690883 844, Merck, Germany) for 10 min in an ultrasonic bath (Isolab, Germany). We prepared a 10:1 ratio of PDMS (Sylgard 184, Sigma-Aldrich, Germany) and waited for 1 h at room temperature. Glass slides were treated with 100 W air plasma at 0.5 mbar for 2 min using a plasma system (ZEPTO, Diener, Germany) only for PDMS coating. Either uncured PDMS or 3D printer clear resin (FLGPCL02) was coated on glass slides using a spin coater (WS-400B-6NPP/LITE, Laurell Technologies Company, USA) [Fig. 1(a)]. For this purpose, PDMS and resin were first spread on the glass slides at 500 rpm for 10 s, and then the spin rate was elevated to the final speed, where it

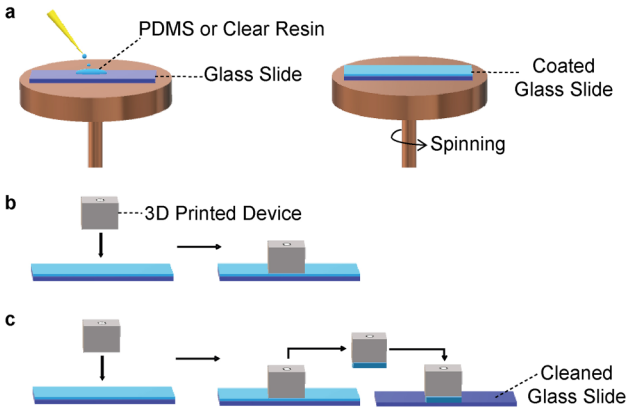

FIG. 1. Adhesive bonding strategies. (a) Adjusting thicknesses of adhesive interlayers. Clean glass slides are coated with PDMS/clear resin using different spinning speeds. (b) Direct bonding technique. 3D printed device is placed directly on the coated glass slides. (c) Transfer bonding technique. 3D printed device is placed on the coated glass slides, and then this device is transferred and put on a second glass slide. PDMS/clear resin layers between the 3D printed device and the glass slide are then cured to achieve sealed microfluidic channels.

Published under license by AIP Publishing.

remained for 20 s. Different final spin speeds (1000 rpm–4000 rpm) were used to reach different final coating thicknesses. At this stage, 3D-printed channels could either be put directly on the coated glass slides [direct bonding technique, Fig. 1(b)] or be placed on the coated glass slides and then transferred to clean glass slides [transfer bonding technique, Fig. 1(c)]. We cured assembled pieces with a PDMS interlayer at 80 °C for 12 h. The resin interlayer was cured with UV exposure at a wavelength of 370 nm using 36 W UV box (JD-818, Yani Minicure Supplies Company, China). Different exposure times to cure the resin interlayer were tested (Fig. S1 in the supplementary material). Since 10 s exposure time shows good bonding even for the thick resin interlayers spin coated at 1000 rpm, this exposure time was chosen to be used for different resin thicknesses. By doing so, sealed microfluidic channels were achieved.

C. Characterization of fabricated channels

For bonding strength tests, we printed cylindrical chambers with 2.5 mm radius, 1 mm height, and a single inlet with a diameter of 1.4 mm and its corresponding mold (Fig. S2 in the supplementary material). 3D-printed chambers were sealed on glass slides with the presented bonding strategy. The PDMS chamber was also fabricated by pouring 10:1 PDMS mixture on the 3D-printed mold and then curing at 80 °C for 12 h. After cooling PDMS to room temperature, the inlet was opened with a needle with 1.4 mm inner diameter (C3 Technology, Turkey) on the chamber. Then, we sealed PDMS on a glass slide after treating the bonding surfaces with 100 W air plasma at 0.5 mbar for 2 min. Tubing with 0.508 mm inner diameter and 1.016 mm wall thickness (Tygon® Saint-Gobain, USA) was connected to the chamber inlet, and then the inlet was sealed with epoxy (Pattex, Australia) for an airtight connection. We applied compressed air from 1 bar to 10 bar with 0.5 bar incremental steps on these chambers through tubing for a duration of 2 min for each pressure value (Fig. S3 in the supplementary material). Red food color solution (Ozmen Food Products, Turkey) was also injected into the tubing in order to visualize possible leakages inside chambers under a Zeiss Axio Vert A1 inverted fluorescence microscope (ZEISS, Switzerland). The tensile test was also performed on the bonded channels (Fig. S4 in the supplementary material). To do so, we attached the 3D-printed cylindrical chamber on a glass slide with transfer bonding technique using 1000 rpm coated resin interlayer. Chocks were bonded on the prepared sample with epoxy, and a classical tensile test was conducted using a Shimadzu AGS-J 5kN test device (Shimadzu, USA).

After bonding the 3D-printed channel to a glass slide, sealed channel height was measured and compared to initial 3D-printed channel height. To do so, channels with 800 μm (width) × 400 μm (height) cross section were designed and fabricated. Microscopy imaging capability of fabricated microfluidic channels was investigated using red food color solution and 10–20 μm fluorescent green (excitation at 470 nm and peak emission at 505 nm) and red (excitation at 550 nm and peak emission at 605 nm) microspheres (Cospheric LLC, CA, USA). Channels were inspected under the inverted microscope equipped with 5× and 20× objectives, bright-field illumination, Zeiss Colibri 7 Type RGB-UV LED fluorescent illumination (385/30 nm, 469/38 nm, 555/30 nm, and 631/33 nm excitation bandwidths), and Zeiss filter set FS 90 HE (Fig. S5 in the supplementary material). We calculated the fluorescence intensity of a microsphere using ImageJ software by subtracting mean fluorescence of the microsphere from mean fluorescence of the background. Same fluorescent intensity (20%) and exposure time (600 ms) were used for the fluorescent inspection of all fabricated channels.

D. Protein immobilization and characterization

After the glass slide was cleaned with 70% ethanol in the ultrasonic bath for 10 min, it was dried with N_2 and treated by 100 W air plasma at 0.5 mbar for 2 min. Then, the glass slide was incubated for 45 min in 4% (v/v) (3-mercaptopropyl) trimethoxysilane (3-MPS) (Sigma-Aldrich, Germany) silanization solution prepared in 200 proof ethanol (Merck, Germany). After the glass slide was rinsed with 1 ml ethanol and dried at room temperature, it was attached to a PDMS chip to make protein patterns on it (Fig. S6 in the supplementary material). A PDMS chip with 1×1 mm^2 cross-sectional channels was fabricated from 3D-printed molds using soft lithography technique. PDMS chip and glass slide were sealed in between two 3D-printed plates screwed to each other (Fig. S7 in the supplementary material). After channels were washed with Phosphate Buffered Saline (PBS) (Thermo Fisher Scientific, USA), 1.2 mg/ml *N*-γ-maleimidobutyryl-oxysuccinimide (GMBS) (Thermo Fisher Scientific, USA) solution was injected inside channels and incubated for 45 min in a dark environment. The channels were cleaned with PBS and then 0.2 mg/ml Protein-G (Thermo Fisher Scientific, USA) solution was introduced into channels and incubated for overnight at 4 °C. This Protein-G immobilization protocol was adapted from Inan *et al.*[34] After the channels were rinsed with PBS and dried with N_2, the glass slide was detached from the PDMS chip. Then, the glass slide was bonded to a 3D-printed chip with 1×1 mm^2 cross-sectional channels using transfer bonding technique, where 1000 rpm spin coated resin is utilized. Afterward, 1% (w/v) Bovine Serum Albumin (BSA) (Sigma-Aldrich, Germany) solution prepared in PBS was incubated inside the channels for 30 min. Channels were washed with 0.1% (w/v) Pluronic F-127 (Sigma-Aldrich, Germany) solution prepared in PBS, and then 50 μg/ml goat anti-mouse IgG (H + L) antibody labeled with Alexa Fluor™ Plus 488 (Thermo Fisher Scientific, USA) was introduced into the channels and incubated for 30 min. Channels were rinsed with 0.1% Pluronic solution, and fluorescence intensities were measured on Protein-G patterns using the inverted microscope. Same protocol was also applied for the PDMS chip, which was used instead of a 3D-printed chip. The PDMS chip was attached on the glass slide as in the Protein-G patterning protocol. Using the presented protocol, different fluorescent-labeled antibody concentrations (i.e., 0.01–100 μg/ml goat anti-mouse IgG prepared in 0.1% Pluronic solution) were further analyzed on the 3D-printed chip.

III. RESULTS AND DISCUSSION

First, we analyzed the resolution of the 3D SLA printer by fabricating semi-circular open channels, rectangular open channels, corresponding molds of these open channels, square

Published under license by AIP Publishing.

open channels, and enclosed square channels (Fig. S8 in the supplementary material). After fabrication, resulting channel dimensions were compared with the designed ones (Fig. S9 in the supplementary material). 3D printer showed good linear relation between designed and fabricated channel dimensions. Channels designed to have at least 75 μm and 50 μm heights were successfully printed for semi-circular channels and their corresponding molds, respectively. Fabricated dimensions were smaller than the designed ones. For instance, the resulting heights of 75 μm semi-circular channels and their 50 μm mold were 25 μm and 23.4 μm, respectively. For rectangular channels with 2:1 (width: height) aspect ratio, channels and their molds were designed to have 75 μm and 50 μm heights and were also fabricated using the 3D printer. The resulting dimensions were 24.4 μm and 56.1 μm for these channels and molds, respectively. 100 μm square channels were also fabricated as channels with 134.2 μm width and 38.3 μm height. The fabricated channel height was ~2.5-fold less than the designed square channels (<400 μm). On the other hand, the channel width was nearly same as the designed square channel width. As the designed channel height exceeds 400 μm, the fabricated height becomes comparable with the designed channel height. We also printed enclosed square channels with at least 600 μm channel dimension, but the channels having low channel height (<600 μm) were clogged during the fabrication process. 600 μm enclosed square channels were printed as 670 μm (width) × 975 μm (height). The 3D printer has a z-resolution of 25 μm and a laser spot size of 140 μm, but x–y resolution of the 3D printer is not reported by the manufacturer. Hence, the printed device resolution can be altered for different designs and channel dimensions as observed in Figs. S8 and S9 in the supplementary material.

3D printer clear resin is composed of methacrylic acid esters and a photoinitiator. The printed structures show hydrophobic nature as PDMS and become hydrophilic after air plasma treatment (Fig. S10 in the supplementary material). For instance, before air plasma treatment, the surface contact angle of the printed substrates was 97.5°, whereas it was 15.9° and 105.7° for glass and PDMS substrates, respectively. After air plasma treatment, the surface contact angle was reduced to 29.7°, 6.3°, and 4.5° for printed, glass, and PDMS substrates, respectively.

Direct and transfer bonding strategies were used to fabricate a microfluidic chip by adhering 3D-printed open microfluidic channels to glass substrates with the PDMS/resin adhesive interlayer (Fig. 1). The effect of interlayer thicknesses to bonding quality was analyzed. To achieve different interlayer thicknesses, PDMS/resin was coated on the glass slides at various spinning speeds [Figs. 2(a) and 2(b)]. For instance, 10–110 μm thick PDMS/resin can be obtained on the glass slides using 1000–4000 rpm spinning speeds. Since the resin can be accumulated on a glass slide by time (Fig. S11 in the supplementary material) due to its hydrophobic nature, the resin was used immediately just after spin coating to get well-defined interlayer thickness. After the fabrication of microfluidic chips with different interlayer thicknesses [Fig. 2(c)], pressurized air was applied on the chips and bonding strength was analyzed by monitoring leakages [Fig. 2(d)]. Bonding strength reached 8.8 bar and 8.6 bar for direct bonding technique using 1000 rpm spin coated PDMS and resin interlayers, respectively [Fig. 2(e)]. A similar bonding strength value (9.1 bar) was obtained for 1000 rpm spin coated resin for transfer bonding technique. This bonding strength is twofold larger than the bonding strength value (4.5 bar) of a PDMS/glass chip fabricated using a traditional plasma bonding technique. In addition, presented transfer bonding technique with a resin interlayer provides at least twofold more bonding strength than the other bonding strategies presented in the literature (Table S1 in the supplementary material). We also evaluated the bonding strength of chips fabricated with transfer bonding technique using tensile stress test and found that the microfluidic chip can withstand up to 9.6 bar [Fig. 2(f)], which is comparable to the bonding strength value obtained with pressurized air. On the other hand, bonding strength can only reach to 3.6 bar while using 1000 rpm spin coated PDMS interlayer for transfer bonding. Thickness of the interlayer affects the bonding quality. For instance, low PDMS thicknesses used in direct bonding resulted in low bonding strength values. For resin interlayer, low resin thickness (<55 μm) can severely decrease bonding quality, resulting in a maximum bonding strength of 1 bar. However, for transfer bonding, similar bonding strength values were found for different PDMS thicknesses down to 20 μm. Presented direct and transfer bonding techniques cannot work with ~10 μm thick interlayers spin coated at 4000 rpm. We tried to apply clamping in order to provide uniform pressure to the bonding surface (Fig. S12 in the supplementary material) but still observed no bonding for thin interlayers.

We evaluate the effect of bonding strategy on resulting channels. To do so, open channels designed as 800 μm (width) × 400 μm (height) cross section were printed and bonded to glass slides with direct and transfer bonding strategies. Resulting channels with 1000 rpm and 2000 rpm spin coated PDMS interlayers were clogged during the bonding process (Fig. S13 in the supplementary material). 1000 rpm spin coated resin interlayers showed clogging inside the channels fabricated using direct bonding strategy (Fig. S13 in the supplementary material). On the other hand, channels fabricated using transfer bonding strategy with 1000 rpm spin coated resin interlayers were fully functional [Fig. 3(a)], and resulting channel heights were slightly (0.48%) smaller compared to the 3D-printed open channel heights [Fig. 3(b)]. For channels fabricated with 3000 rpm spin coated PDMS interlayers using direct and transfer bonding strategies and with 2000 rpm spin coated resin interlayers using direct bonding strategy, their heights increased about 5.7%, 1.27%, and 0.48%, compared to their initial heights [Fig. 3(b)]. Transfer bonding strategy with 1000 rpm spin coated resin interlayers enables fully functional channels designed as 250 × 250 μm^2 cross section [Fig. 3(c)] resulted in a 280 μm (width) × 110 μm (height) channel profile (Fig. S14 in the supplementary material). Resulting channel dimensions were similar to the initial channel profiles just before the bonding process (Fig. S15 in the supplementary material). However, the channels having lower dimensions (<250 μm) were completely clogged after the bonding process (Fig. S16 in the supplementary material). As shown in Table S1 in the supplementary material, the presented bonding technique allows the fabrication of transparent channels having lower micro-scale dimensions than the other 3D-printed fabrication techniques

Published under license by AIP Publishing.

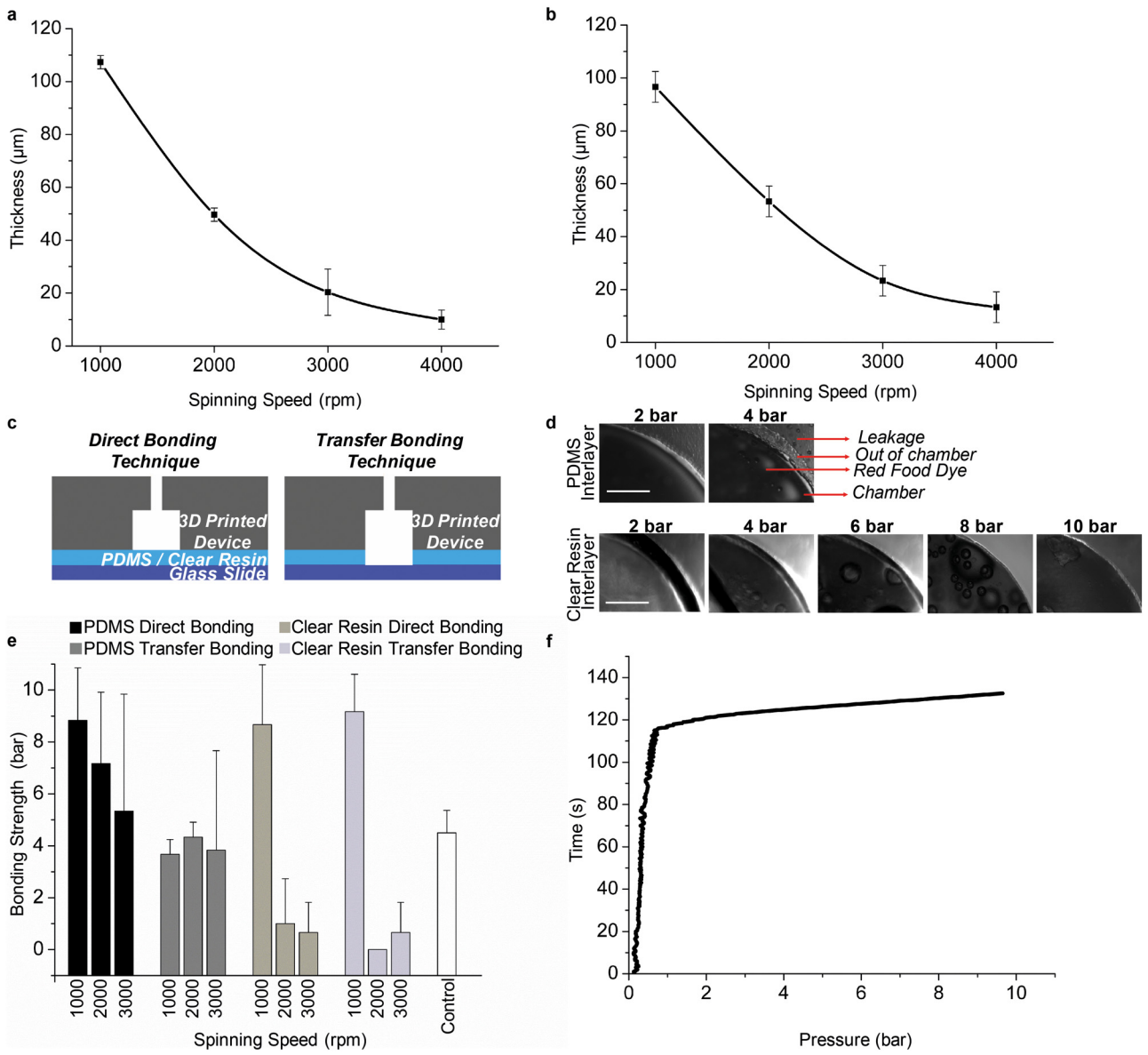

FIG. 2. Bonding strength tests. (a) PDMS and (b) clear resin thicknesses obtained using different spinning speeds. (c) Cross-sectional views of direct and transfer bonding strategies to fabricate the microfluidic chamber for bonding strength tests. (d) Micrographs of microfluidic chips after applying different pressure values. The chips are fabricated using a 1000 rpm spin coated PDMS/resin interlayer with transfer bonding strategy, and microfluidic chambers are filled with red food color solution for visualization. Scale bars are 200 μm. (e) Bonding strength values of direct and transfer bonding strategies where different spinning speeds are used for the PDMS/resin interlayer. Control indicates PDMS/glass chips fabricated using traditional plasma bonding technique. (f) Tensile stress test of a microfluidic chip fabricated using transfer bonding strategy with 1000 rpm spin coated resin.

using an affordable 3D printer (<3500$). With the bonding strategy, we utilized the maximum resolution capacity of the 3D printer using open channel designs, as these designs could be printed successfully in lower dimensions compared to enclosed channel designs (Figs. S8 and S9 in the supplementary material).

Optical transparency of fabricated microfluidic channels was tested with red food color and microsphere solutions. 800 μm (width) × 400 μm (height) channels were fabricated using direct and transfer bonding strategies as described above. For comparison, the PDMS/glass chip (control) with 800 μm (width) × 400 μm (height) rectangular channels and monolithic

Published under license by AIP Publishing.

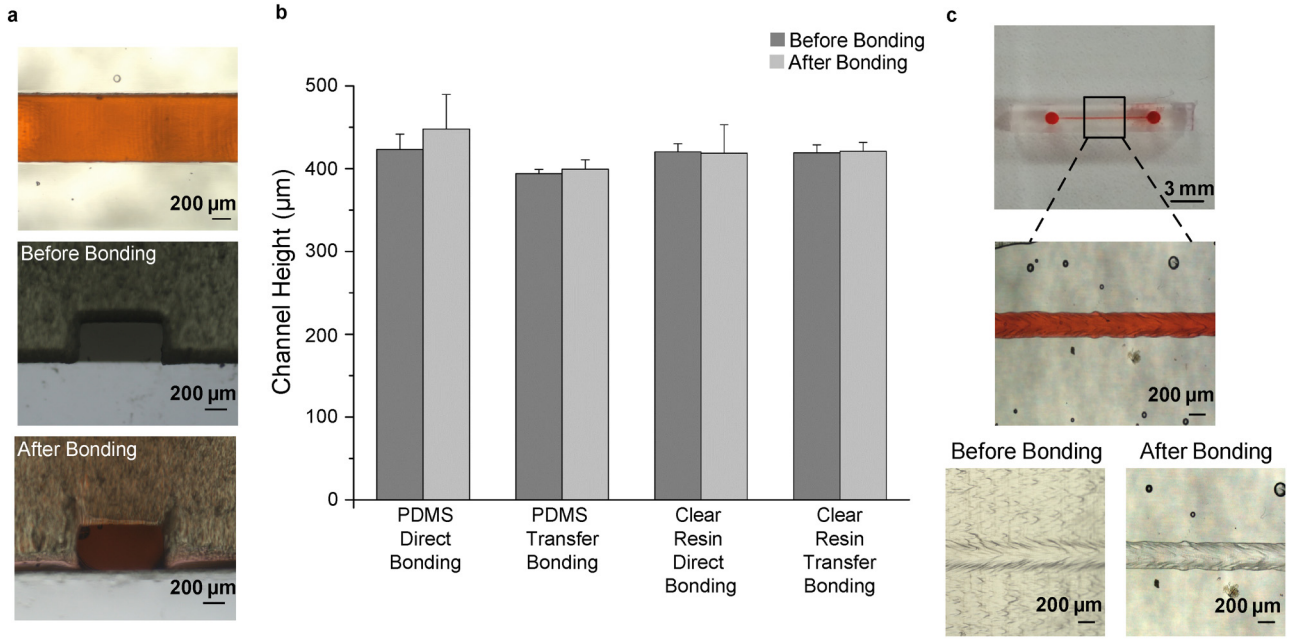

FIG. 3. Profiles of bonded channels. (a) Top and cross-sectional views of a microfluidic channel. 3D printed open channel designed as 800 μm (width) × 400 μm (height) cross-sectional profile is bonded on a glass slide using transfer bonding strategy with a 1000 rpm spin coated resin interlayer. (b) Corresponding heights of the microfluidic channels before and after the bonding processes. (c) Photographs of a fabricated microfluidic channel. The open channel designed to have 250 × 250 μm^2 cross section is printed and bonded to a glass slide using transfer bonding strategy with 1000 rpm spin coated resin. The bonded channel is filled with red food color solution for visualization.

3D-printed enclosed channels with $600 \times 600\,\mu m^2$ cross section were designed. The thicknesses of devices were set to be the same for all channels (i.e., total 6 mm with 5 mm top layer composed of a PDMS/3D-printed material and 1 mm bottom layer composed of a glass slide/3D-printed material). As shown in Fig. 4(a), red food color solution is visible to the naked eye in all channels fabricated using different strategies. However, neither red food color solution nor the microspheres in the 3D-printed enclosed channels were clearly imaged under the microscope [Figs. 4(b) and 4(d)]. Since bottom layers of the bonded channels were composed of perfectly optically clear glass slides, fluorescent and bright-field intensity values of 3D-printed enclosed channels could be lower compared to bonded devices. We also tested the imaging capability of the monolithic 3D-printed enclosed channel by increasing light intensities. Although bright-field intensity was increased 2.5-fold, the channel was not clearly visible (Fig. S17 in the supplementary material). Increasing fluorescent intensity about fivefold did not help to clearly observe fluorescent microspheres (Fig. S18 in the supplementary material). On the other hand, the presented bonding strategies allowed bright-field and fluorescence imaging [Figs. 4(c) and 4(d)]. Fluorescence intensities of red and green microspheres were evaluated in the channels. The intensity profiles of red fluorescent microspheres in the fabricated channels are statistically different from the intensity profiles in the control channels ($p < 0.0001$). The red fluorescent intensities are 0.65- to 0.72-fold lower in the fabricated channels compared to the control channels. On the other hand, intensity profiles of green fluorescent microspheres are statistically indifferent ($p > 0.05$) in the fabricated channels compared to the control ones [Figs. 4(e) and 4(f)]. Although red fluorescent sensitivity slightly decreases in the fabricated channels, probably due to background autofluorescence issues in 3D-printed materials,[35] the fabricated channels can be used for red and green fluorescence imaging applications as traditional PDMS/glass channels. Hence, our fabrication strategy can also allow a broad range of imaging applications in 3D microfluidic devices with its bright field and fluorescent imaging capabilities (Table S1 in the supplementary material).

Fabrication of microfluidic chips using transfer bonding strategy with 1000 rpm spin coated resin interlayer ensures fast processing time (30 s for spin coating and 10 s for UV exposure), room temperature sealing, superior bonding strength value (>9 bar), small channel dimensions ($\leq 280\,\mu m$), and channel transparency for bright-field and fluorescence microscopy. If microfluidic chips are fabricated with glass surfaces having protein patterns by using this bonding strategy, it can enhance the use of these monolithic chips by allowing many different imaging applications including multiplex biomarker analysis. We evaluated the effect of bonding on the performance of Protein-G patterns on glass slides by

Published under license by AIP Publishing.

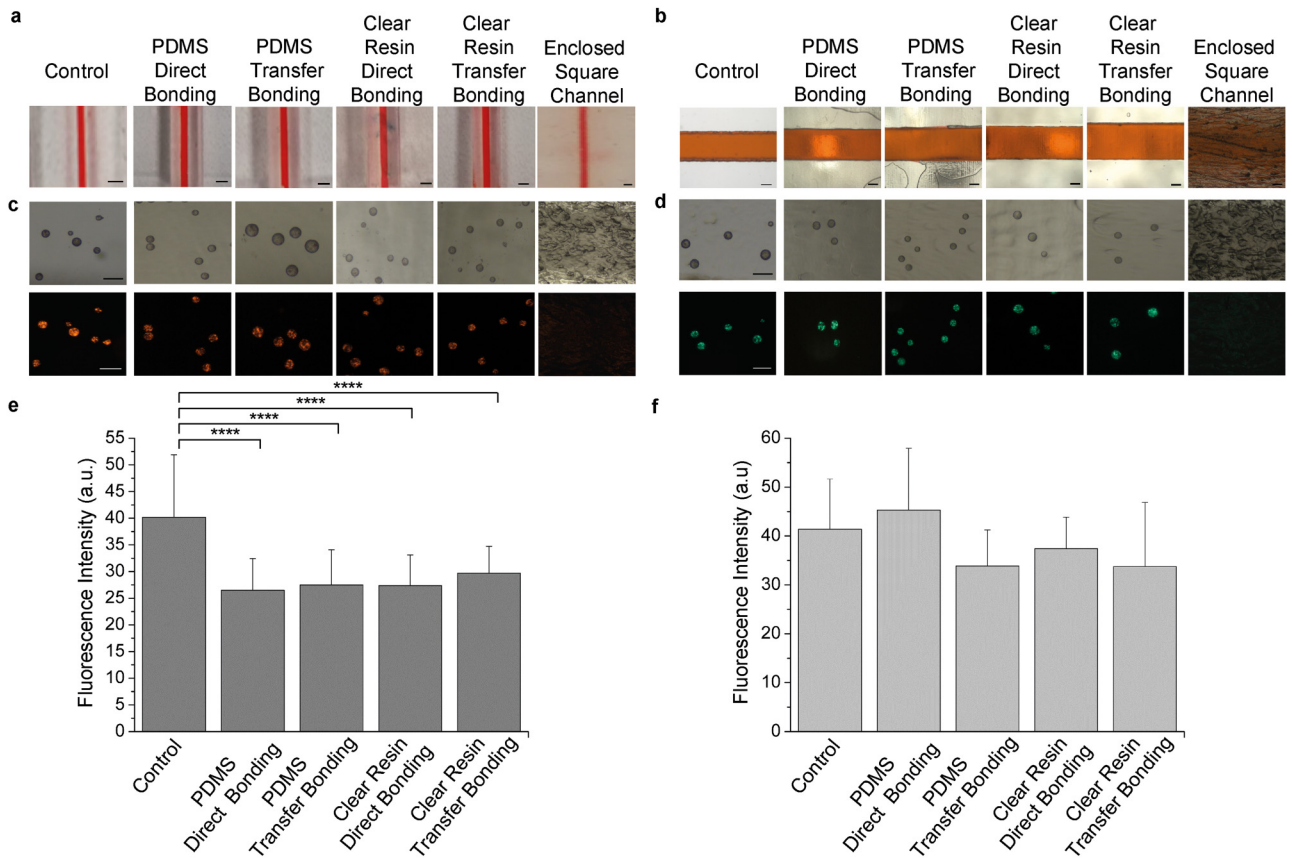

FIG. 4. Imaging of the fabricated channels. (a) Photographs and (b) micrographs of the channels filled with red flood color solution. Scale bars are 1 mm and 200 μm for photographs and micrographs, respectively. Micrographs are taken with 5× objective. (c) and (d) Bright-field and fluorescence micrographs of red and green microspheres taken with 20× objective. Scale bars are 50 μm. (e) and (f) Fluorescence intensity values of red and green microspheres. One-way ANOVA combined with Newman–Keuls multiple comparisons test is used to statistically analyze data. Fluorescence intensities in bonded chips are compared with control (PDMS/glass) chips, and (****) indicates $p < 0.0001$.

labeling them with fluorescence tagged IgG (H + L) antibody inside the bonded channel [Fig. 5(a)]. Fluorescence intensity profiles on Protein-G patterns are statistically indifferent ($p > 0.05$) for the PDMS chip (i.e., the PDMS channel clamped to the glass slides) and the 3D-printed chip (i.e., the 3D-printed open channel bonded on the glass slides using transfer bonding strategy with a 1000 rpm spin coated resin interlayer), as shown in Fig. 5(b). IgG antibodies are highly specific to Protein-G, and this can be observed as a higher fluorescence intensity profile on the Protein-G pattern compared to the BSA pattern and bare Protein-G pattern (i.e., without fluorescent antibodies). UV illumination can damage proteins depending on the illumination dose.[36] Since low power UV-A source (36 W) and short illumination period (10 s) are used for bonding, the resulted low UV dose (i.e., 0.36 kJ for 100% energy conversion efficiency) is not expected to affect the functionality of Protein-G. A high UV-A dosing (i.e., 18.8 kJ for 3 min exposure) was also studied on antibody-antigen binding kinetics, and this dosing did not show any adverse effect on binding.[37] Hence, the presented bonding strategy can be used safely to integrate protein patterns inside microfluidic channels without altering functionality of proteins, while fully 3D-printed enclosed channels and bonding strategies with chemical surface treatment/material coating do not allow the integration of protein patterns in microfluidic devices (Table S1 in the supplementary material). Furthermore, microfluidic channels with Protein-G patterns, which were fabricated using transfer bonding technique with 1000 rpm resin interlayer, were used to detect fluorescent IgG antibodies spiked in PBS. The increasing antibody concentration resulted in high fluorescence intensity on the Protein-G pattern [Fig. 5(c)]. We calculated the limit of detection (LOD) value as ~30 ng/ml by intersecting the linear fit curve of the experimental data with the LOD signal (i.e., mean plus 3 standard deviation of a reference experiment with 0 g/ml IgG).[8] Hence, our fabrication strategy enables detection of low concentration of molecules with fluorescent labels, which can be suitable for different biosensing applications.

Published under license by AIP Publishing.

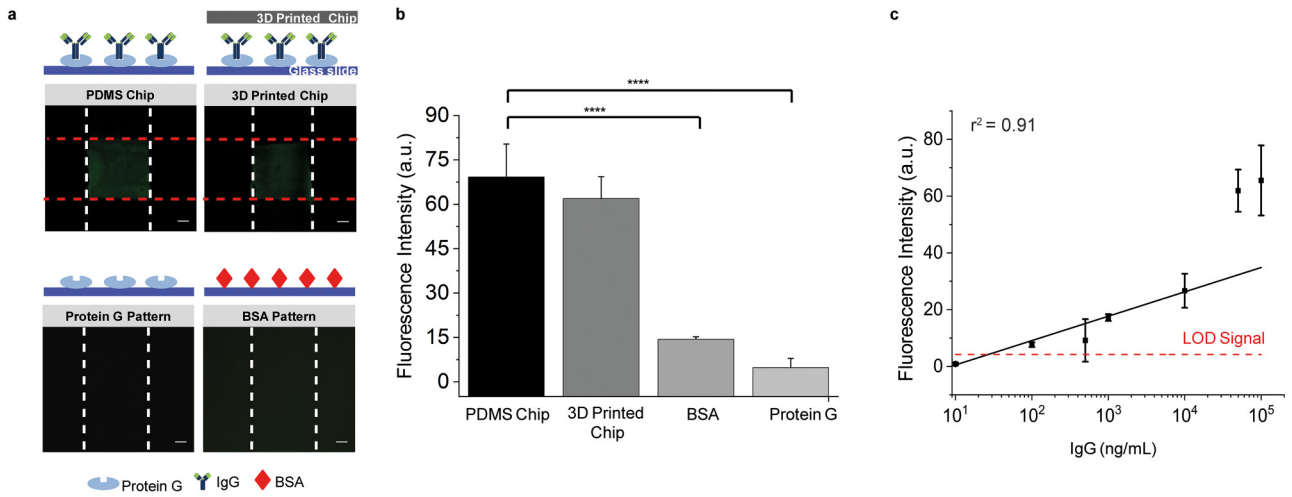

FIG. 5. Analysis of protein patterns. (a) Fluorescence micrographs and (b) corresponding mean fluorescence intensity values of protein patterns in PDMS and 3D-printed chips. Protein-G and BSA patterns are labeled with fluorescent IgG antibody. Before labeling in the PDMS chip, bare Protein-G pattern is analyzed. PDMS chip is also used to analyze the BSA pattern. Protein patterns of the PDMS chip are inspected after unclamping the PDMS channel from the glass slides. Protein patterns and channels are in between white and red dashed lines, respectively. Scale bars are 200 μm. Data are statistically analyzed using one-way ANOVA combined with the Newman–Keuls multiple comparisons test. Fluorescence intensities in different cases are compared with PDMS chips, and (****) indicates $p < 0.0001$. (c) Log plot of IgG concentration and the corresponding fluorescent signal on the Protein-G pattern inside the 3D-printed microfluidic chip. Linear fit to the data with a coefficient of determination (r^2) is shown in the figure.

IV. CONCLUSION

Although SLA printers ensure high-resolution printing of structures with minimum 25 μm, this technology can only fabricate monolithic channels having dimensions equal to and larger than 600 μm since the resin clogging issues and the fabricated channels are not suitable for microscopy imaging due to their limited transparency. As shown in Table S1 in the supplementary material, the presented fabrication strategy allows fabrication of transparent microfluidic channels with dimensions down to $280 \times 110\ \mu m^2$ using an affordable 3D printer (<3500$), which could only previously be achieved using microstreolithography[28] and expensive SLA printers[25] with custom-made printing materials. Moreover, fabricated chips with the presented bonding strategies enable bright-field and fluorescence microscopy imaging. The resulting bonding strength varies based on interlayer materials and thicknesses. Nevertheless, the achieved bonding strength can be more than twofold higher than the traditional PDMS/glass bonding with plasma treatment and other bonding strategies applied for 3D-printed channels (Table S1 in the supplementary material). The transfer bonding strategy with a resin interlayer has the advantage of short processing time (<1 min), room temperature operation, and easy integration of secondary substrates. Although other 3D microfluidic device fabrication strategies can affect the secondary substrate surface with long, high-temperature, and wet printing and bonding process conditions, we showed that protein functionalized surfaces could be integrated into monolithic chips without damaging their functionality. Hence, the presented adhesive bonding strategies enhance optical imaging capabilities of 3D-printed microfluidic devices and also allow them to be used for fluorescent-based protein detection purposes. We think that the presented bonding strategies will disseminate the usage of 3D-printed microfluidic devices in a broad range of imaging applications.

SUPPLEMENTARY MATERIAL

See the supplementary material for Figs. S1–S18 and Table S1. The electronic supplementary file includes Fig. S1, The curing of clear resin with different UV exposure times; Fig. S2, Fabrication of the chamber for bonding strength tests; Fig. S3, Setup for bonding strength tests; Fig. S4, Tensile test setup; Fig. S5, Illustration of the inverted microscope used for the inspection of fabricated microfluidic devices; Fig. S6, Illustration of the protein patterning process; Fig. S7, PDMS chip structure for Protein-G patterning; Fig. S8, Micrographs of 3D-printed channels and their molds; Fig. S9, Relation between designed and corresponding fabricated channel dimensions; Fig. S10, Surface contact angle measurements; Fig. S11, Time dependent distribution of resin; Fig S12, Photograph of the 3D-printed device clamped to the glass slide with binder clips; Fig. S13, Micrographs of clogged channels having 800 μm width and 400 μm height fabricated using direct and transfer bonding techniques with different interlayers; Fig. S14, Cross-sectional image of a bonded microfluidic channel designed as $250 \times 250\ \mu m^2$ using scanning electron microscopy; Fig. S15, 3D-printed open channels designed as $250 \times 250\ \mu m^2$; Fig. S16, Micrographs of clogged channels; Fig. S17, Bright-field micrograph of the 3D-printed enclosed channel filled with red food color solution; Fig. S18, Fluorescent micrograph of microspheres inspected in the

Published under license by AIP Publishing.

3D-printed enclosed channel. Table S1, Comparison of strategies for fabricating transparent microfluidic devices.

AUTHOR'S CONTRIBUTIONS

All authors contributed equally to this work.

ACKNOWLEDGMENTS

H.C.T. acknowledges financial support from The Scientific and Technological Research Council of Turkey (Grant Nos. 116M298 and 217S518). The authors would like to thank Engin Ozcivici, Ph.D. from the Department of Bioengineering, Izmir Institute of Technology (IZTECH) and the group members of the Laboratory of Biomedical Micro and Nanosystems (LBMS), IZTECH for helpful discussions. The authors would like to thank also Serdar Ozcelik, Ph.D., Canan Varlıklı, Ph.D., and Halide Diker, Ph.D. from the Department of Photonics, IZTECH for their support on spin coating; Metin Tanoglu, Ph.D., Serkan Kangal, and Zeynep Ay from the Department of Mechanical Engineering, IZTECH for their support on tensile tests and contact angle measurements; and the IZTECH Center for Materials Research (CMR) for SEM analysis. The authors also specially thank Betul Karakuzu, Oyku Beytorun, and Pinar Buse Taskiran from LBMS for their kind support in the experiments.

DATA AVAILABILITY

The data that support the findings of this study are available from the corresponding author upon reasonable request.

REFERENCES

[1]C. M. B. Ho, S. H. Ng, K. H. H. Li, and Y.-J. Yoon, "3D printed microfluidics for biological applications," Lab Chip **15**(18), 3627–3637 (2015).
[2]S. Ng and Z. Wang, "Hot roller embossing for microfluidics: Process and challenges," Microsyst. Technol. **15**(8), 1149–1156 (2009).
[3]H. C. Tekin, V. Sivagnanam, A. T. Ciftlik, A. Sayah, C. Vandevyver, and M. A. Gijs, "Chaotic mixing using source–sink microfluidic flows in a PDMS chip," Microfluid. Nanofluid. **10**(4), 749–759 (2011).
[4]A. K. Au, N. Bhattacharjee, L. F. Horowitz, T. C. Chang, and A. Folch, "3D-printed microfluidic automation," Lab Chip **15**(8), 1934–1941 (2015).
[5]Y. Hwang, O. H. Paydar, and R. N. Candler, "3D printed molds for non-planar PDMS microfluidic channels," Sens. Actuators A **226**, 137–142 (2015).
[6]Y. Xia and G. M. Whitesides, "Soft lithography," Angew. Chem. Int. Ed. **37**(5), 550–575 (1998).
[7]I. E. Araci and S. R. Quake, "Microfluidic very large scale integration (mVLSI) with integrated micromechanical valves," Lab Chip **12**(16), 2803–2806 (2012).
[8]H. C. Tekin, M. Cornaglia, and M. A. Gijs, "Attomolar protein detection using a magnetic bead surface coverage assay," Lab Chip **13**(6), 1053–1059 (2013).
[9]R. Sochol, E. Sweet, C. Glick, S. Venkatesh, A. Avetisyan, K. Ekman, A. Raulinaitis, A. Tsai, A. Wienkers, and K. Korner, "3D printed microfluidic circuitry via multijet-based additive manufacturing," Lab Chip **16**(4), 668–678 (2016).
[10]D. Qin, Y. Xia, and G. M. Whitesides, "Soft lithography for micro-and nanoscale patterning," Nat. Protoc. **5**(3), 491 (2010).
[11]R. Amin, S. Knowlton, A. Hart, B. Yenilmez, F. Ghaderinezhad, S. Katebifar, M. Messina, A. Khademhosseini, and S. Tasoglu, "3D-printed microfluidic devices," Biofabrication **8**(2), 022001 (2016).
[12]A. I. Shallan, P. Smejkal, M. Corban, R. M. Guijt, and M. C. Breadmore, "Cost-effective three-dimensional printing of visibly transparent microchips within minutes," Anal. Chem. **86**(6), 3124–3130 (2014).
[13]S. Waheed, J. M. Cabot, N. P. Macdonald, T. Lewis, R. M. Guijt, B. Paull, and M. C. Breadmore, "3D printed microfluidic devices: Enablers and barriers," Lab Chip **16**(11), 1993–2013 (2016).
[14]B. C. Gross, J. L. Erkal, S. Y. Lockwood, C. Chen, and D. M. Spence, *Evaluation of 3D Printing and Its Potential Impact on Biotechnology and the Chemical Sciences* (ACS Publications, 2014).
[15]N. Bhattacharjee, A. Urrios, S. Kang, and A. Folch, "The upcoming 3D-printing revolution in microfluidics," Lab Chip **16**(10), 1720–1742 (2016).
[16]K. G. Lee, K. J. Park, S. Seok, S. Shin, J. Y. Park, Y. S. Heo, S. J. Lee, and T. J. Lee, "3D printed modules for integrated microfluidic devices," RSC Adv. **4**(62), 32876–32880 (2014).
[17]K. B. Anderson, S. Y. Lockwood, R. S. Martin, and D. M. Spence, "A 3D printed fluidic device that enables integrated features," Anal. Chem. **85**(12), 5622–5626 (2013).
[18]J. M. Lee, M. Zhang, and W. Y. Yeong, "Characterization and evaluation of 3D printed microfluidic chip for cell processing," Microfluid. Nanofluid. **20**(1), 5 (2016).
[19]C. Chen, B. T. Mehl, A. S. Munshi, A. D. Townsend, D. M. Spence, and R. S. Martin, "3D-printed microfluidic devices: Fabrication, advantages and limitations—a mini review," Anal. Methods **8**(31), 6005–6012 (2016).
[20]F. Li, N. P. Macdonald, R. M. Guijt, and M. C. Breadmore, "Increasing the functionalities of 3D printed microchemical devices by single material, multimaterial, and print-pause-print 3D printing," Lab Chip **19**(1), 35–49 (2019).
[21]B. C. Gross, K. B. Anderson, J. E. Meisel, M. I. McNitt, and D. M. Spence, "Polymer coatings in 3D-printed fluidic device channels for improved cellular adherence prior to electrical lysis," Anal. Chem. **87**(12), 6335–6341 (2015).
[22]V. Romanov, R. Samuel, M. Chaharlang, A. R. Jafek, A. Frost, and B. K. Gale, "FDM 3d printing of high-pressure, heat-resistant, transparent microfluidic devices," Anal. Chem. **90**(17), 10450–10456 (2018).
[23]A. K. Au, W. Lee, and A. Folch, "Mail-order microfluidics: Evaluation of stereolithography for the production of microfluidic devices," Lab Chip **14**(7), 1294–1301 (2014).
[24]F. Kotz, P. Risch, D. Helmer, and B. E. Rapp, "Highly fluorinated methacrylates for optical 3D printing of microfluidic devices," Micromachines **9**(3), 115 (2018).
[25]H. Gong, M. Beauchamp, S. Perry, A. T. Woolley, and G. P. Nordin, "Optical approach to resin formulation for 3D printed microfluidics," RSC Adv. **5**(129), 106621–106632 (2015).
[26]C. I. Rogers, K. Qaderi, A. T. Woolley, and G. P. Nordin, "3D printed microfluidic devices with integrated valves," Biomicrofluidics **9**(1), 016501 (2015).
[27]N. Bhattacharjee, C. Parra-Cabrera, Y. T. Kim, A. P. Kuo, and A. Folch, "Desktop-stereolithography 3D-printing of a poly (dimethylsiloxane)-based material with sylgard-184 properties," Adv. Mater. **30**(22), 1800001 (2018).
[28]F. Kotz, K. Arnold, W. Bauer, D. Schild, N. Keller, K. Sachsenheimer, T. M. Nargang, C. Richter, D. Helmer, and B. E. Rapp, "Three-dimensional printing of transparent fused silica glass," Nature **544**(7650), 337–339 (2017).
[29]L. J. Y. Ong, A. Islam, R. DasGupta, N. G. Iyer, H. L. Leo, and Y.-C. Toh, "A 3D printed microfluidic perfusion device for multicellular spheroid cultures," Biofabrication **9**(4), 045005 (2017).
[30]J. Cheon and S. Kim, "Intermediate layer-based bonding techniques for polydimethylsiloxane/digital light processing 3D-printed microfluidic devices," J. Micromech. Microeng. **29**(9), 095005 (2019).
[31]S. Zips, O. J. Wenzel, P. Rinklin, L. Grob, K. Terkan, N. Y. Adly, L. Weiß, and B. Wolfrum, "Direct stereolithographic 3D printing of microfluidic structures on polymer substrates for printed electronics," Adv. Mater. Technol. **4**(3), 1800455 (2019).
[32]E. Wilhelm, C. Neumann, K. Sachsenheimer, T. Schmitt, K. Länge, and B. E. Rapp, "Rapid bonding of polydimethylsiloxane to stereolithographically manufactured epoxy components using a photogenerated intermediary layer," Lab Chip **13**(12), 2268–2271 (2013).
[33]E. Hamad, S. Bilatto, N. Adly, D. Correa, B. Wolfrum, M. J. Schöning, A. Offenhäusser, and A. Yakushenko, "Inkjet printing of UV-curable adhesive and dielectric inks for microfluidic devices," Lab Chip **16**(1), 70–74 (2016).

Published under license by AIP Publishing.

[34]H. Inan, J. L. Kingsley, M. O. Ozen, H. C. Tekin, C. R. Hoerner, Y. Imae, T. J. Metzner, J. S. Preiss, N. G. Durmus, and M. Ozsoz, "Monitoring neutropenia for cancer patients at the point of care," Small Methods **1**(9), 1700193 (2017).
[35]G. I. Salentijn, P. E. Oomen, M. Grajewski, and E. Verpoorte, "Fused deposition modeling 3D printing for (bio) analytical device fabrication: Procedures, materials, and applications," Anal. Chem. **89**(13), 7053–7061 (2017).
[36]A. C. Eischeid and K. G. Linden, "Molecular indications of protein damage in adenoviruses after UV disinfection," Appl. Environ. Microbiol. **77**(3), 1145–1147 (2011).
[37]Y. M. Shirshov, A. Majstrenko, P. Smertenko, and E. Surovtseva, "Direct observation of UV-B radiation effect on antigen–antibody coupling using surface plasmon resonance," Sens. Actuators B **105**(2), 290–294 (2005).

Published under license by AIP Publishing.